

# Delineating the Impact of Diluent on High-Concentration Electrolytes for Developing High-Voltage $\text{LiNi}_{0.5}\text{Mn}_{1.5}\text{O}_4$ Spinel Cathode

Jiayi Zhang, Orion Cohen, Xiuyao Lang, Boyu Wang, Stephen E. Trask, Kyeongjae Cho, Kristin A. Persson,\* and Laisuo Su\*

$\text{LiNi}_{0.5}\text{Mn}_{1.5}\text{O}_4$  (LNMO) is a high-voltage spinel cathode with low nickel content, making it an attractive candidate for next-generation lithium-ion batteries (LIBs). However, its application is limited by interfacial instability with conventional carbonate-based electrolytes at high voltages. In this work, a localized saturated electrolyte (LSE) capable of stably operating up to 4.85 V is investigated. Molecular dynamics simulations and Fourier transform infrared spectroscopy reveal that adding “non-solvating” 1,1,2,2-tetrafluoroethyl-2,2,3,3-tetrafluoropropyl ether diluent in the saturated electrolyte, more  $\text{PF}_6^-$  anions are present in the first solvation shell of  $\text{Li}^+$ , at the expense of solvent molecules. This tailored solvation environment promotes the formation of a robust, LiF-rich cathode-electrolyte interphase that mitigates transition metal dissolution and parasitic side reactions. The optimized LSE enables excellent cycling performance, with 95% capacity retention in  $\text{Li}|\text{LNMO}$  half-cells after 100 cycles and 94% retention in  $\text{Li}_4\text{Ti}_5\text{O}_{12}|\text{LNMO}$  full cells after 250 cycles, even at a practically relevant LNMO cathode loading of  $\approx 15 \text{ mg cm}^{-2}$ . These results highlight the benefits of electrolyte engineering and solvation structure control in advancing high-voltage LIB technologies.

## 1. Introduction

Layered transition metal oxides such as  $\text{LiCoO}_2$ ,  $\text{LiNi}_x\text{Mn}_y\text{Co}_{1-x-y}\text{O}_2$ , and  $\text{LiNi}_x\text{Co}_y\text{Al}_{1-x-y}\text{O}_2$  have been commonly used in lithium-ion batteries (LIBs) for portable energy storage and electric vehicles because of their superior energy density and cycle life.<sup>[1]</sup> Compared to these materials,  $\text{LiNi}_{0.5}\text{Mn}_{1.5}\text{O}_4$  (LNMO) contains more earth-abundant manganese, less expensive nickel, and no toxic cobalt, making it an environmentally friendly and cost-effective choice for cathode materials in LIBs.<sup>[2]</sup> Over the past two decades, LNMO has attracted significant research interest due to its exceptional balance of cost-effectiveness and performance.<sup>[3]</sup> LNMO is characterized by its well-defined  $\text{Li}^+$  migration channels, provided by its spinel structure, allowing for nearly complete delithiation and lithiation with minimal structural change during cycling.<sup>[4,5]</sup> Moreover, its high voltage plateau at 4.7 V (vs  $\text{Li}/\text{Li}^+$ ) allows it to deliver a high

energy density of  $650 \text{ Wh kg}^{-1}$  (compared with  $734 \text{ Wh kg}^{-1}$  for  $\text{LiCoO}_2$ ,  $400 \text{ Wh kg}^{-1}$  for  $\text{LiMn}_2\text{O}_4$ , and  $495 \text{ Wh kg}^{-1}$  for  $\text{LiFePO}_4$ ).<sup>[6]</sup> However, the high operating voltage accelerates side reactions between LNMO and electrolytes, leading to fast capacity degradation and safety issues.<sup>[7]</sup> Various strategies have been reported to tackle the challenge, including element doping,<sup>[8,9]</sup> surface coating,<sup>[10–13]</sup> morphology control,<sup>[14–16]</sup> binder engineering,<sup>[17–19]</sup> and electrolyte engineering.<sup>[20–23]</sup> Electrolyte engineering is particularly advantageous as it preserves existing battery components and infrastructure, making it a more cost-effective approach compared to developing novel materials for LIBs.<sup>[24]</sup>

The electrolyte decomposition in LNMO-based LIBs occurs in three aspects: non-Faradaic (chemical reactions), Faradaic (electrochemical reactions), and non-redox reactions, in which chemical oxidation is the dominant process that profoundly impacts the surface reactivity and stability of the cathode material.<sup>[7,25]</sup> Conventional electrolytes constituted of lithium hexafluorophosphate ( $\text{LiPF}_6$ ) and organic carbonates such as ethylene carbonate (EC) and ethyl methyl carbonate (EMC), are highly susceptible to decomposition, leading to the production of harmful

J. Zhang, X. Lang, B. Wang, K. Cho, L. Su  
Department of Materials Science and Engineering  
University of Texas at Dallas  
Richardson, Texas 75080, USA  
E-mail: [laisuo.su@utdallas.edu](mailto:laisuo.su@utdallas.edu)

O. Cohen  
Department of Chemistry  
University of California Berkeley  
Berkeley, CA 94720, USA

K. A. Persson  
Department of Materials Science and Engineering  
University of California Berkeley  
Berkeley, CA 94720, USA  
E-mail: [kristinpersson@berkeley.edu](mailto:kristinpersson@berkeley.edu)

S. E. Trask  
Chemical Sciences and Engineering Division  
Argonne National Laboratory  
Lemont, IL 60439, USA

The ORCID identification number(s) for the author(s) of this article can be found under <https://doi.org/10.1002/smll.202502141>

DOI: 10.1002/smll.202502141

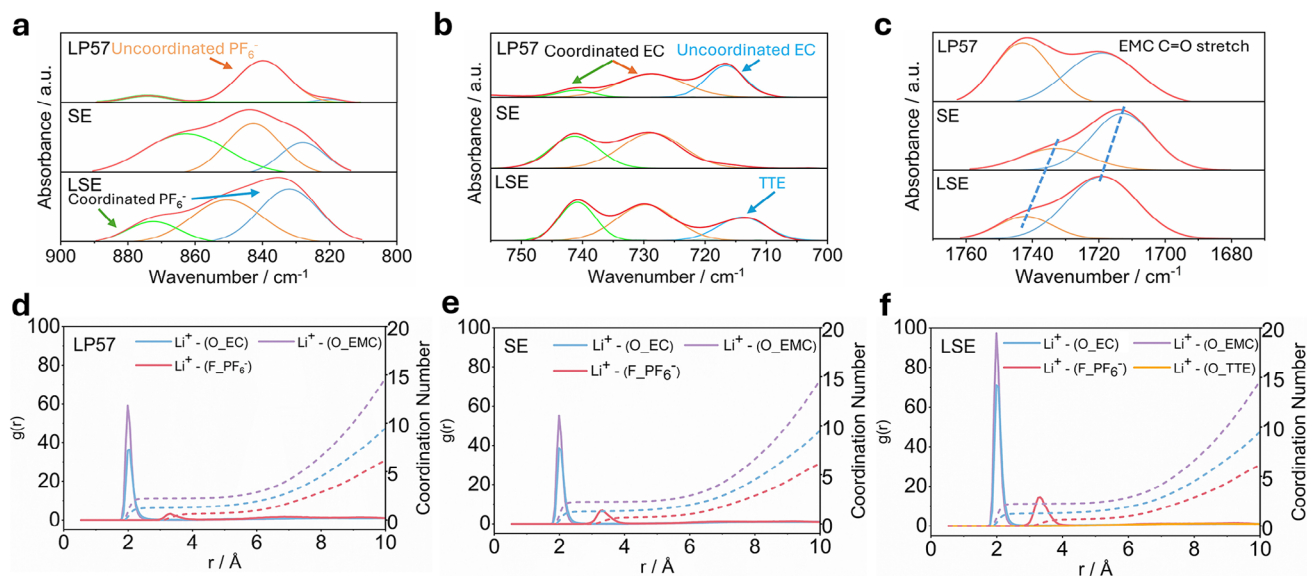


**Figure 1.** a–c) Selected FTIR spectra of the three electrolytes (a) in the region of  $800\text{ cm}^{-1}$  to  $900\text{ cm}^{-1}$  that corresponds to the coordination condition of  $\text{PF}_6^-$ , (b) in the region of  $700\text{ cm}^{-1}$  to  $760\text{ cm}^{-1}$  that corresponds to the coordination condition of EC molecules, and (c) in the region of  $1680\text{ cm}^{-1}$  to  $1800\text{ cm}^{-1}$  that corresponds to the C=O stretching of EMC molecules. d–f) The RDFs of (d) LP57, (e) SE, and (f) LSE obtained from MD simulations.

chemicals like hydrofluoric acid (HF) and phosphorus pentafluoride.<sup>[26]</sup> These acidic species accelerate the transition metal dissolution of LNMO and lead to the formation of thick and resistive cathode electrolyte interphase (CEI).<sup>[27,28]</sup> Altering the composition of free solvent molecules, anions, and cation solvation structures has been shown to effectively optimize side reactions and improve the properties of electrode/electrolyte interphases.<sup>[29,30]</sup>

Recently, novel electrolyte configurations, such as high-concentration electrolytes (HCEs) and localized high-concentration electrolytes (LHCEs), have been shown to offer an alternative promising approach by tailoring solvent molecule interactions and solvation sheath structures in LIB electrolytes.<sup>[31,32]</sup> HCEs enhance LIB performance by reducing the number of free solvent molecules, thereby minimizing side reactions and improving stability.<sup>[33]</sup> Similarly, LHCEs are built on HCEs by adding non-solvating diluents to reduce the viscosity of the electrolyte with little impact on the  $\text{Li}^+$  solvation structure.<sup>[34,35]</sup> However, the design of HCEs and LHCEs often involves the usage of expensive, high-solubility lithium salts (e.g., lithium bis(fluorosulfonyl)imide), which limits their commercial application. A viable alternative solution is to use low-cost lithium salts to create localized saturated electrolytes (LSEs), which accords with the demand for a cost-effective solution for designing affordable electrolytes.<sup>[36]</sup> In the presence of a diluent, the  $\text{LiPF}_6$  and carbonate solvents (like EC, and EMC) constructed a unique solvation structure in the electrolyte, which improved the cycle stability of layered-structure high-voltage cathode materials ( $\text{LiNiO}_2$ ,<sup>[36,37]</sup>  $\text{LiCoO}_2$ ,<sup>[38]</sup> and  $\text{LNi}_{0.7}\text{Mn}_{0.25}\text{Al}_{0.05}\text{O}_2$ <sup>[39]</sup>) in lithium metal batteries.<sup>[40]</sup>

The applicability of LSE has not been demonstrated with cathode electrodes beyond 4.6 V, and the solvation structure of LSE has not been theoretically explored to uncover the  $\text{Li}^+$  solvation structure. It is, therefore, worthwhile to further explore the ap-

plicability of LSE in high-voltage LNMO cathodes with an operational voltage up to 4.85 V. In this work, we study the solvation structure of LSE with a combination of experimental techniques and molecular dynamics (MD) simulation and illustrate the effectiveness of the electrolyte in protecting spinel LNMO at a deep charging cut-off voltage of 4.85 V vs  $\text{Li}^+/\text{Li}$ . X-ray photoelectron spectroscopy (XPS) analysis is conducted for cycled LNMO cathode and Li anode. Our findings illustrate the mechanisms underlying the localized saturated effect and provide insight into electrolyte design for LIBs.

## 2. Results and Discussion

### 2.1. Solvation Structures Analysis of Localized Saturated Effect

The baseline electrolyte is LP57 with a composition of 1 M  $\text{LiPF}_6$  in EC/EMC (3/7, v/v). The saturated electrolyte (SE) has a composition of 3.5 M  $\text{LiPF}_6$  in EC/EMC (3/7, v/v), and the LSE was made by adding two times (by volume) of the non-solvating 1,1,2,2-tetrafluoroethyl-2,2,3,3-tetrafluoropropyl ether (TTE) diluent into the SE.<sup>[36]</sup> To investigate the interactions and coordination dynamics within LP57, SE, and LSE electrolytes, Fourier transform infrared (FTIR) spectroscopy (Figures 1a–c; S1, Supporting Information) and MD simulations (Figure 1d–f; Figure S2–S5, Supporting Information) were performed.

Figure S1 (Supporting Information) shows a full spectrum of the FTIR data for the three electrolytes. The two peaks at  $\approx 1720\text{ cm}^{-1}$  and  $1750\text{ cm}^{-1}$  come from the C=O stretching in the EMC molecule. The two peaks at  $700\text{--}760\text{ cm}^{-1}$  are associated with EC coordination, while the two peaks at  $800\text{--}900\text{ cm}^{-1}$  are associated with  $\text{PF}_6^-$ .<sup>[36]</sup> Compared to the peaks in LP57, the positions and intensities of these peaks are all changed in SE and LSE, indicating a change of  $\text{Li}^+$  interactions with these solvents and  $\text{PF}_6^-$  anion. Figure 1a shows the FTIR data that represents

the interactions between  $\text{Li}^+$  and  $\text{PF}_6^-$ , where the peak at  $835\text{ cm}^{-1}$  corresponds to uncoordinated  $\text{PF}_6^-$  ions, and the peaks at  $820\text{ cm}^{-1}$  and  $870\text{ cm}^{-1}$  are characteristic peaks of coordinated  $\text{PF}_6^-$  ions.<sup>[36]</sup> The absorbance peaks at  $820\text{ cm}^{-1}$  and  $870\text{ cm}^{-1}$  are more pronounced in SE and LSE compared to that in the LP57 electrolyte, indicating more  $\text{PF}_6^-$  anions are coordinated with  $\text{Li}^+$  in SE and LSE. The increase in coordinated  $\text{PF}_6^-$  in SE is caused by the increase in  $\text{LiPF}_6$  concentration that shifts the equilibrium of  $\text{LiPF}_6$  desolvation.<sup>[41]</sup> Our findings also align with recent studies that reported that non-solvating diluents can still modulate the  $\text{Li}^+$  solvation shell by altering the spatial and dielectric environment, even though they do not directly coordinate with  $\text{Li}^+$  and this steric and dielectric interference allowing more  $\text{PF}_6^-$  to enter the primary solvation shell.<sup>[42]</sup> Moreover, the vibrational band observed from  $700\text{--}760\text{ cm}^{-1}$  can be attributed to the breathing vibrations of the EC solvent molecules in Figure 1b.<sup>[36]</sup> The peak at  $715\text{ cm}^{-1}$  represents the uncoordinated EC, while the peaks at  $728\text{ cm}^{-1}$  and  $742\text{ cm}^{-1}$  are identified as signatures of coordinated EC molecules. Compared to the LP57 electrolyte, the increased intensity of peaks at  $728\text{ cm}^{-1}$  and  $742\text{ cm}^{-1}$  in SE and LSE suggests that more EC molecules are coordinated with  $\text{Li}^+$ , which can be correlated to its high dielectric constant.<sup>[43,44]</sup> Compared to the FTIR spectra of SE and LSE, there are some differences, especially in the range of  $1600\text{ cm}^{-1}$  to  $1810\text{ cm}^{-1}$  where TTE has no impacts (Figure 1c).<sup>[36]</sup> Thus, adding non-solvating TTE diluent changes  $\text{Li}^+$  solvation structures in SE. To understand the changes, we further carried out MD simulations for the three electrolytes.

Figure 1d–f shows the radial distribution functions (RDFs) of  $\text{Li}^+$  derived from MD simulations of the three electrolyte systems. The ratio of the peak intensity between  $\text{Li}^+(\text{F}_{\text{PF}_6^-})$  and  $\text{Li}^+(\text{O}_{\text{EMC}})$  increased from 0.055 in LP57 to 0.123 and 0.148 in SE and LSE, respectively, indicating enhanced anion-coordination, e.g. where  $\text{PF}_6^-$  anions are in the first solvation shell of  $\text{Li}^+$ . The result agrees with the FTIR data shown in Figure 1a that shows more  $\text{PF}_6^-$  anions are coordinated with  $\text{Li}^+$ . Moreover, the ratio of the peak intensity between  $\text{Li}^+(\text{O}_{\text{EC}})$  and  $\text{Li}^+(\text{O}_{\text{EMC}})$  increased from 0.61 in LP57 to 0.70 and 0.73 in SE and LSE, respectively, indicating that more EC molecules are in the first solvation shell of  $\text{Li}^+$  in SE and LSE. The different RDFs in SE and LSE confirm that adding non-solvating TTE diluent changes the  $\text{Li}^+$  solvation structures in SE.

From the MD simulations, we obtained the  $\text{Li}^+$  coordination number of each solvent that corresponds to the average number of solvent molecules located in the first solvation shell of  $\text{Li}^+$  (Figure 2a). Compared to the LP57, the coordination number of  $\text{PF}_6^-$  anions increases significantly in SE and LSE, while the coordination number of EMC generally decreases in both electrolytes. However, the coordination number of EC does not change significantly in the three electrolytes. Thus, the major change of  $\text{Li}^+$  solvation structure in the LP57 electrolyte when increasing  $\text{LiPF}_6$  salt concentration is the replacement of EMC molecules by  $\text{PF}_6^-$  anions around the  $\text{Li}^+$ . When comparing SE and LSE, the coordination number of  $\text{PF}_6^-$  anions further increases in LSE, while the coordination numbers of EMC and EC slightly decrease. Thus, adding TTE diluent in SE promotes the formation of anion coordination, mainly at the expense of EMC and EC coordination.

The coordination number represents an average result of the  $\text{Li}^+$  solvation structure. In an electrolyte, there is typically a major-

ity species (e.g.,  $\text{Li}^+$  solvated entirely by solvents) as well as many minority species corresponding to various anion and solvent-coordinated  $\text{Li}^+$  solvation structures. Figure S4 and Tables S1–S4 (Supporting Information) show the major  $\text{Li}^+$  solvation structures and their fractions present in the three electrolytes. It is worth noting that the most dominating  $\text{Li}^+$  solvation structures are similar in the three electrolytes, which are 1EC-3EMC (1  $\text{Li}^+$  is surrounded by 1 EC molecule and 3 EMC molecules) and 2EC-2EMC (1  $\text{Li}^+$  is surrounded by 2 EC molecules and 2 EMC molecules). However, the ratios of the anion-containing  $\text{Li}^+$  solvation structures, such as 1 $\text{PF}_6^-$ -1EC-2EMC, increase in SE and LSE. Figure 2b summarizes the top five anion-containing  $\text{Li}^+$  solvation structures present in the three electrolytes. The sum of them in the LSE reaches 53%, which is higher than both SE (47%) and LP57 (18%). Thus, the non-solvating TTE diluent affects the  $\text{Li}^+$  solvation structure in electrolytes. Our result agrees with the recent finding that the addition of the non-solvating diluents affects the solvation structure of  $\text{Li}^+$  cations in the LHCEs.<sup>[45,46]</sup>

The fraction of free molecules and anions corresponding to their total amount in different electrolytes is illustrated in Figure 2c. Compared to LP57, the free molecules of all species (EC, EMC,  $\text{PF}_6^-$ ) are reduced because of the increased salt concentration. Interestingly,  $\approx 98\%$  of TTE molecules are free in LSE and only 2% of the TTE molecules are involved in the  $\text{Li}^+$  solvation, which agrees with the low dielectric constant of the TTE molecules. However, the 2% of TTE molecules that appear in the  $\text{Li}^+$  solvation structure may have a non-negligible impact. For example, the proportion of free  $\text{PF}_6^-$  anion in LSE (38.6%) is lower than that in SE (43.8%), which is caused by the 2% coordinated TTE molecules. In addition, the free EC and EMC molecule ratios are slightly increased in LSE (29.6%, 20.4%) compared to SE (28.6%, 16.5%). These results further confirmed that with the non-solvating TTE solvent, more  $\text{PF}_6^-$  is coordinated with  $\text{Li}^+$  while solvent molecules are pushed out. It is worth noting that the coordinating environment of  $\text{Li}^+$  is dynamic with a fast exchange between solvating molecules and non-solvating molecules. 2% of the solvating TTE molecules is a statistical average value for those that appear in the first solvation shell of  $\text{Li}^+$  over time. In Figure S5 (Supporting Information), the ratios of the coordinated molecules vs the randomly selected molecules show that the chance of obtaining coordinated solvent molecules and  $\text{PF}_6^-$  in LSE is larger than that in SE and LSE.

Three different types of  $\text{Li}^+$  solvation structures have been proposed to describe different  $\text{Li}^+$  environments, including solvent-separated ion pairs (SSIPs,  $\text{Li}^+$  and  $\text{PF}_6^-$  are not in direct contact with each other), contact ion pairs (CIPs, a  $\text{PF}_6^-$  anion coordinating with one  $\text{Li}^+$ ), and cation-anion aggregates (AGGs, a  $\text{PF}_6^-$  anion coordinating to two or more  $\text{Li}^+$ ). Figure 2d shows that the  $\text{Li}^+$  solvation structure changes significantly from LP57 to SE and LSE. The ratio of SSIP is reduced from 82.5% in LP57 to 59.1% in SE and 58.1% in LSE, while the ratio of CIP is increased from 15.8% in LP57 to 27.3% in SE and 28.7% in LSE. Similarly, the ratio of AGG also increased from 1.7% in LP57 to 13.2% in SE and 13.1% in LSE. Figure 2e displays the schematic of the change of the  $\text{Li}^+$  solvation environment from LP57 to SE and LSE. By increasing the  $\text{LiPF}_6$  salt concentration in LP57, more CIP and AGG are formed in the SE due to the reduced amount of free solvent. When adding “non-solvating” TTE diluent in SE, more  $\text{PF}_6^-$  anions are present in the first solvation shell of  $\text{Li}^+$ , at the

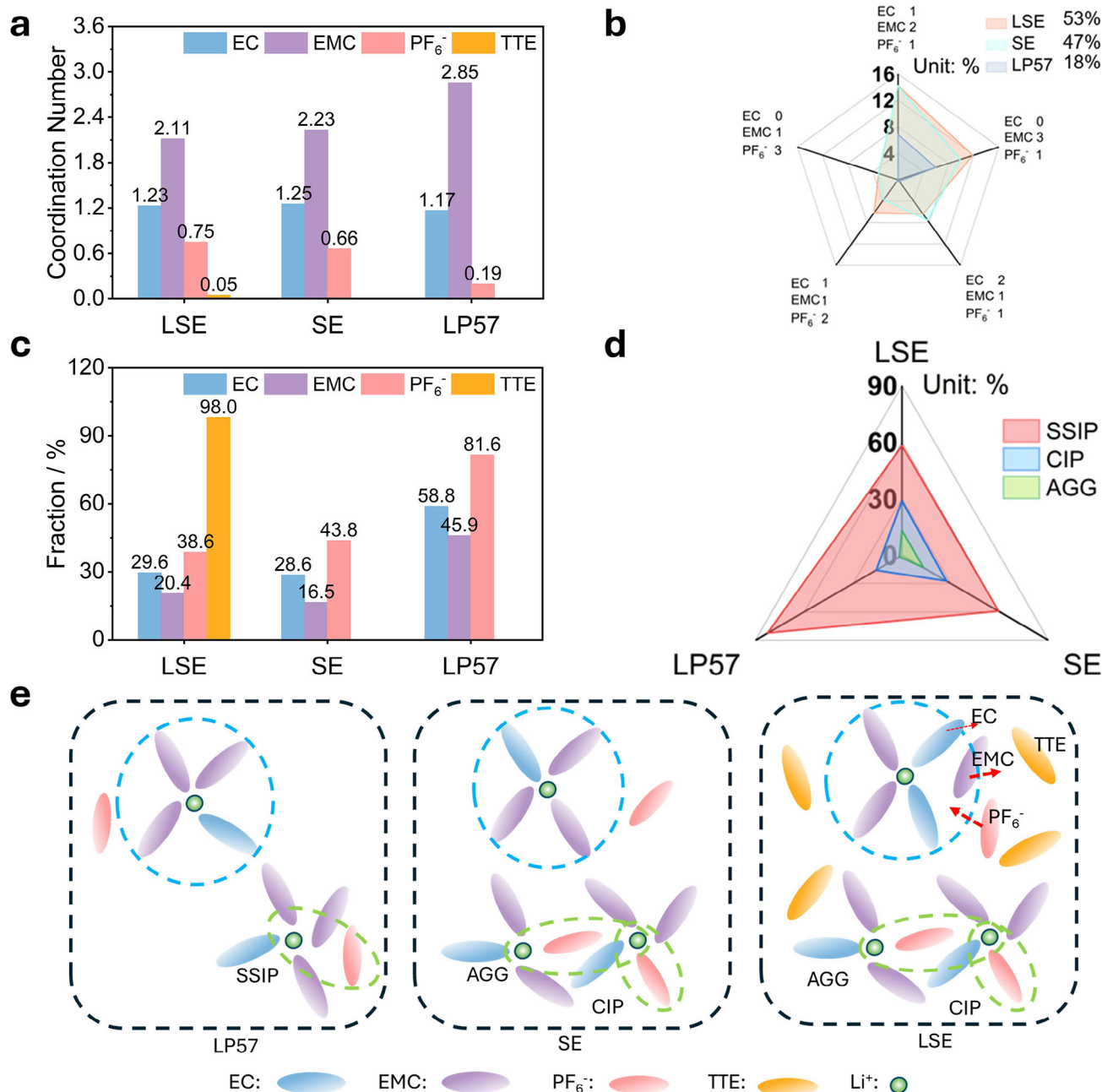


**Figure 2.** a) The coordination number of solvent, anion, and diluent with Li<sup>+</sup> in the three investigated electrolytes. b) The fraction of different PF<sub>6</sub><sup>-</sup> containing solvation structures in three electrolytes. c) The percentage of solvents, anions, and diluents in electrolytes that are not bound to Li<sup>+</sup>. d) The fraction of SSIP, CIP, and AGG structures in electrolytes. e) The schematics illustrate the change in solvation structures and the impact of diluent on the solvation structure.

expense of EC and EMC coordination. Compared to EC, more EMC molecules are pushed out in the SE after adding TTE diluent which may be correlated to its relatively low dielectric constant.<sup>[47]</sup> It is worth noting that in our previous study, EC is pushed out in the Gen2 electrolyte (1.2 M LiPF<sub>6</sub> in EC/EMC) when PF<sub>6</sub><sup>-</sup> anion enters the first Li<sup>+</sup> solvation shell because of the electrostatic repulsion between the highly polarizable EC and the negatively charged PF<sub>6</sub><sup>-</sup> anion.<sup>[48]</sup> Therefore, the interaction between Li<sup>+</sup> and solvent molecules (e.g., EC and EMC) depends

on various factors such as the concentration of anion and the existence of diluent.

Figure S6 (Supporting Information) presents a dominant <sup>7</sup>Li nuclear magnetic resonance signal with a clear upfield shift in SE, which suggests shorter Li<sup>+</sup>-PF<sub>6</sub><sup>-</sup> distances resulting from the formation of CIPs and AGGs at higher salt concentrations.<sup>[49]</sup> Moreover, the LSE displays broader and asymmetric line shapes, suggesting the presence of a second lithium environment that undergoes slow exchange with the primary Li<sup>+</sup> species observed

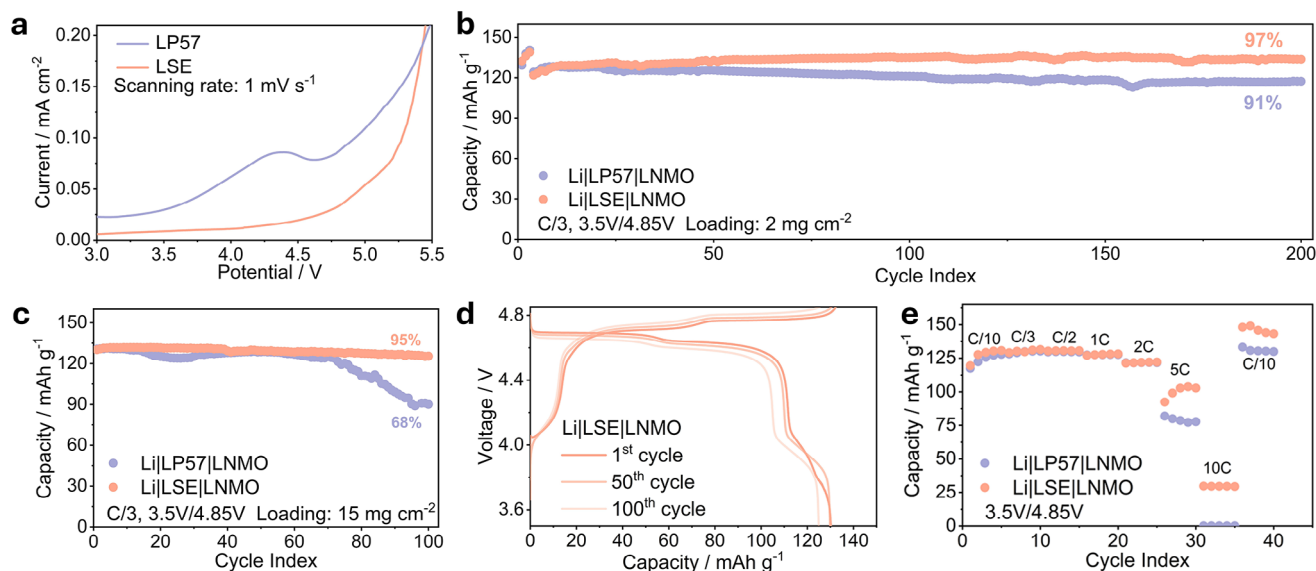


**Figure 3.** a) The linear sweep voltammetry results of LP57 and LSE tested in Li|Al cell. b,c) Cycling performance of Li|LNMO half-cells with LP57 electrolyte and LSE at room temperature with (b)  $2 \text{ mg cm}^{-2}$  loading and (c)  $15 \text{ mg cm}^{-2}$  loading of the cathode active material. d) The charge and discharge curves of Li|LNMO cells tested with LSE after different numbers of cycles. e) The rate performance of Li|LNMO cells in two electrolytes.

in LP57. Notably, this spectral asymmetry is absent in the SE samples, implying that the TTE diluent influenced the  $\text{Li}^+$  solvation structure by altering its solvation environment. The combined results from FTIR spectroscopy and MD simulations provide a comprehensive understanding of the solvation structure modifications induced by the addition of the diluent in the electrolyte. FTIR analysis reveals a shift in the  $\text{Li}^+$ -solvent interaction, indicating a decrease in the presence of EMC within the primary solvation shell. MD simulations further confirm this observation by showing that the introduction of the diluent enhances  $\text{PF}_6^-$  coordination with  $\text{Li}^+$ , which in turn leads to the displacement of EMC molecules from the first solvation shell. This consistent trend observed across both experimental and computational approaches underscores that the diluent plays an active role in restructuring the  $\text{Li}^+$  solvation environment, rather than merely acting as an inert component to reduce the viscosity of the electrolyte.

## 2.2. Electrochemical Properties of LSE and Its Compatibility with LNMO Cathode

The unique solvation structure in LSE increases its high-voltage stability. Figure 3a shows that the oxidative stability is increased from  $\approx 4.0 \text{ V}$  in LP57 to  $4.75 \text{ V}$  (vs  $\text{Li}/\text{Li}^+$ ). The stability tests were conducted in Li|Al cells and the result cannot always represent the stability of these electrolytes in actual cells. Nevertheless, the result suggests the LSE is more oxidatively stable than the baseline LP57 electrolyte. To evaluate the compatibility of LSE with a high-voltage LNMO cathode, Li|LNMO half-cells were assembled with different cathode mass loadings. Figure 3b shows the cycling performance of Li|LNMO cell with a LNMO electrode mass loading of  $2 \text{ mg cm}^{-2}$ . The cells with both electrolytes have a similar discharge capacity of  $136 \text{ mAh g}^{-1}$  at C/3. The capacity retention increased from 91% in LP57 electrolyte to 97% in LSE after 200 cycles.

A more practical cathode loading of  $15 \text{ mg cm}^{-2}$  was further evaluated in Li|LNMO cells. Figure 3c shows that the LNMO cathode electrodes exhibited an initial discharge capacity of  $134 \text{ mAh g}^{-1}$  in both electrolytes. The capacity retention of the high-loading LNMO electrode is increased from 68% in LP57 electrolyte to 95% in LSE after 100 cycles. A fast capacity fading was observed for the cell with the LP57 electrolyte after 70 cycles. Figure S7 (Supporting Information) shows that the voltage hysteresis of the cell increases significantly after 70 cycles, which could be from the poor compatibility between the electrolyte and Li metal anode. The average Coulombic efficiency (CE) of the half cell with LSE remains above 99.6% throughout 100 cycles, while the LP57-based cell exhibits a gradually decreasing CE starting from  $\sim 99.2\%$  and falling below 98.5% after 80 cycles. (Figure S8, Supporting Information). Figure 3d shows the charge and discharge curves of the Li|LNMO half-cells tested at C/3 in LSE. The charge-discharge plateaus at  $\approx 4.7 \text{ V}$  and  $4.8 \text{ V}$  correspond to the  $\text{Ni}^{2+}/\text{Ni}^{3+}$  and  $\text{Ni}^{3+}/\text{Ni}^{4+}$  redox couples of the LNMO cathode, and the short plateau at  $\approx 4.15 \text{ V}$  comes from the  $\text{Mn}^{3+}/\text{Mn}^{4+}$  redox couple. All three plateaus are preserved from the first cycle to the 50<sup>th</sup> cycle, while the  $\text{Ni}^{2+}/\text{Ni}^{3+}$  and  $\text{Ni}^{3+}/\text{Ni}^{4+}$  plateaus are slightly shortened at the 100<sup>th</sup> cycle. Similar phenomena can be found in the Li|LNMO cell tested with the LP57 electrolyte (Figure S9, Supporting Information). A closer look at the differential capacity curve ( $dQ/dV$ ) curves of the cells in Figure S10 (Supporting Information) shows that the intensities of two peaks at  $4.7$  and  $4.8 \text{ V}$  gradually reduce, and their positions gradually shift to a larger voltage during charging. The gradually increased overpotential could be from the poor compatibility between the electrolytes and the Li metal anode. Nevertheless, the intensities of the two peaks in the Li|LNMO cell with LSE show a much less reduction compared to that in the LP57 electrolyte, indicating better protection of the LNMO cathode in LSE.

Figure 3e compares the rate capability of the Li|LNMO cells tested in two electrolytes. They showed similar and good capacity

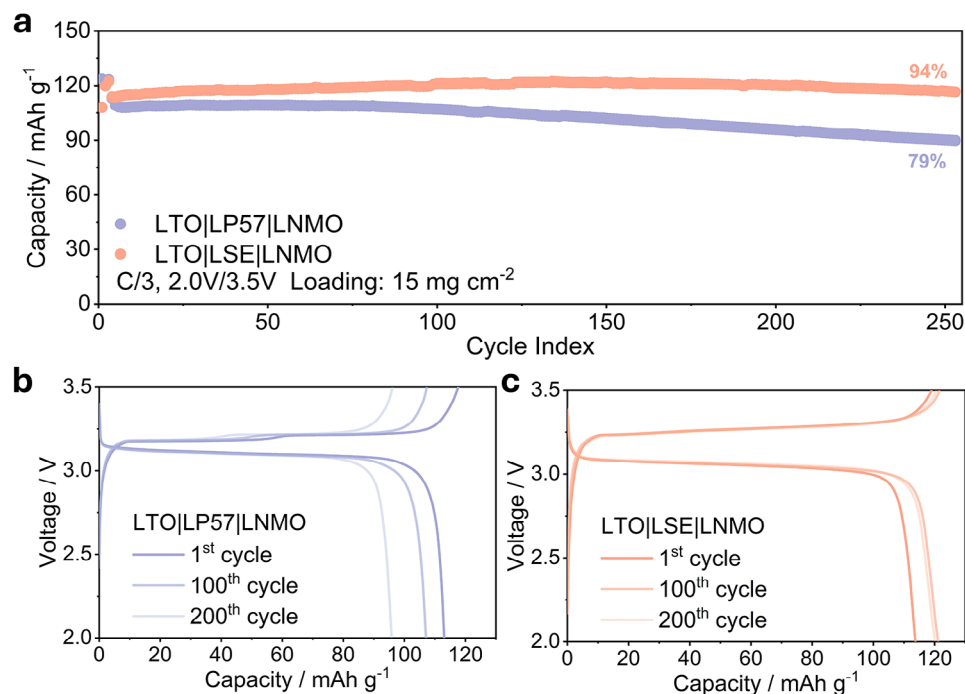


**Figure 4.** a) Cycling performance of LTO|LNMO cells with LP57 electrolyte and LSE. b,c) The charge and discharge curves for LTO|LNMO cells with (b) LP57 electrolyte and (c) LSE.

retention from C/10 to 2C. The capacity remains more than 93% at 2C compared to the maximum achievable capacity at lower C-rates (Figure S11, Supporting Information). The cell tested with LSE shows better capacity retention at high C-rates such as 5C and 10C than the one with the LP57 electrolyte. However, the ionic conductivity of the LSE ( $2.4 \text{ mS cm}^{-1}$ ) is lower than that of the LP57 electrolyte ( $8.7 \text{ mS cm}^{-1}$ ), as measured by electrochemical impedance spectroscopy (EIS) in the Li|Li symmetric cell shown in Figure S12 (Supporting Information). The improved rate capability of the Li|LNMO cell using LSE could be attributed to the increased Li<sup>+</sup> transference number, which rises from 0.38 in LP57 to 0.67 (Figure S13, Supporting Information). Additionally, the formation of a unique interfacial layer, which will be discussed in the following section, may also contribute to this improvement. It needs to be noted that the Li<sup>+</sup> transference number was measured via the Bruce-Vincent method,<sup>[50]</sup> which needs to meet a few conditions such as a diluent electrolyte with no complicated speciation.<sup>[51]</sup> The high concentration of lithium salt in the LSE leads to complicated Li<sup>+</sup> solvation structures that can bring errors when applying the Bruce-Vincent method. A more reliable measurement technique needs to be developed to accurately measure the Li<sup>+</sup> transference number in concentrated electrolytes.

To remove the impact of the Li metal anode in evaluating the compatibility of LSE against LNMO, Li<sub>4</sub>Ti<sub>5</sub>O<sub>12</sub> (LTO) was further selected as the anode because of its well-known stability.<sup>[52]</sup> High-loading LNMO cathode ( $15 \text{ mg cm}^{-2}$ ) was used, and LTO|LNMO full cells were assembled with LP57 and LSE electrolytes. Figure 4a suggests that the LTO|LNMO cell with the LSE shows a maximum discharge capacity of  $122 \text{ mAh g}^{-1}$  at C/3 and retains 94% of its maximum discharge capacity after 250 cycles. In compari-

son, the cell with the baseline LP57 electrolyte only retains 79% of its initial discharge capacity after 250 cycles. We observed a gradual capacity increase in the first 100 cycles for the LTO|LNMO cell with LSE, which could be the slow formation of SEI on the LTO anode and relatively poor permittivity of the LSE into the porous electrodes compared to the LP57 electrolyte. It is reported that trace water and EC molecules in the electrolyte are more likely to decompose and produce gas at the LTO anode during the cycle, and the decomposition products accumulate at the anode to form SEI, and the gas production stops as the SEI stabilizes.<sup>[53,54]</sup>

Figure 4b,c shows the charge and discharge curves of the LTO|LNMO cells tested at C/3 in LP57 and LSE. The charge/discharge plateaus at  $\approx 3.17$  and  $3.25 \text{ V}$  correspond to the Ni<sup>2+</sup>/Ni<sup>3+</sup> and Ni<sup>3+</sup>/Ni<sup>4+</sup> redox couples of the LNMO cathode. Both plateaus are preserved from the first cycle to the 200<sup>th</sup> cycle in LSE while they get shortened in LP57. The cells with LSE achieved a stable CE of  $\approx 99.5\%$  over 250 cycles, while the cells with the LP57 electrolyte exhibited lower CE and increasing variability over time, suggesting that the LSE suppressed parasitic reactions and improved interfacial stability compared to LP57 (Figure S14, Supporting Information). In the dQ/dV analysis (Figure S15, Supporting Information), the shape and position of peaks associated with Ni<sup>2+</sup>/Ni<sup>3+</sup> and Ni<sup>3+</sup>/Ni<sup>4+</sup> redox remain unchanged in LSE while the height of the peaks reduced and the position shifted in LP57. Table S5 (Supporting Information) compares our results with a few recent relevant studies, although there are not that many research articles on developing advanced electrolytes for LTO|LNMO cells. Compared with the few reported data, the LTO|LNMO cells with high-loading LNMO cathode paired with the developed LSE show the best capacity retention. The superior compatibility of LSE in LTO|LNMO

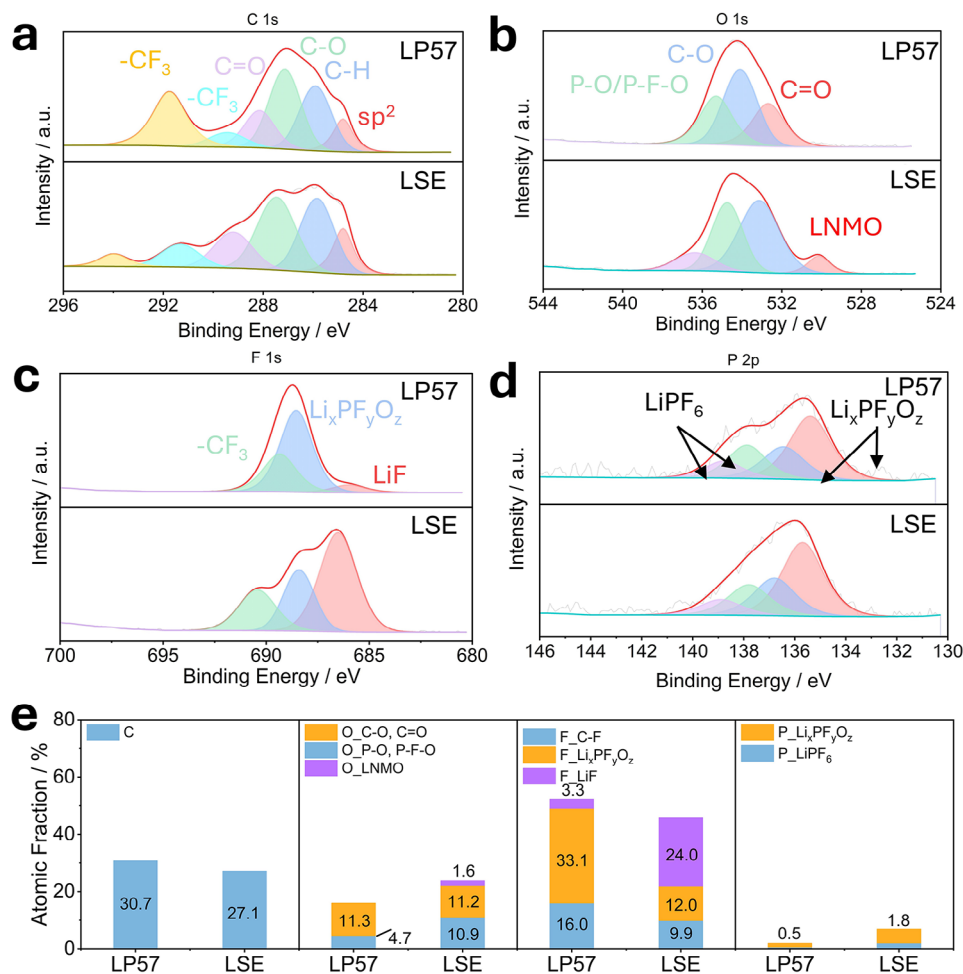


**Figure 5.** XPS characterization of cycled LNMO cathodes. a–d) XPS data of (a) C 1s, (b) O 1s, (c) F 1s, and (d) P 2p for the CEI on the LNMO surface. e) Quantitative analysis of different components derived from the XPS data.

confirmed in our work signified the potential of the application of LTO|LNMO LIBs in practical conditions.

### 2.3. Postmortem Analysis of Cycled LNMO Electrodes

To understand the improved cycling stability of LNMO with the LSE, XPS was employed to characterize the CEI formed on the surface of the cycled LNMO cathodes and the SEI formed on the surface of cycled Li anodes that were harvested from Li|LNMO cells after 200 cycles. **Figure 5a** suggests that various types of carbon-containing components were found on cycled LNMO cathodes tested in the two electrolytes, including conductive carbon (C–C and C–H at  $\approx 284.8$  eV), carbonates (C–O at  $\approx 286.5$  eV and C=O at  $\approx 289.0$  eV), and polyvinylidene fluoride (PVDF) binder (CF<sub>2</sub>–CH<sub>2</sub> at  $\approx 287.5$  eV and C–F at  $\approx 291$  eV). The relative amount of carbon species shown in **Figure 5e** is higher in the CEI formed in LP57 electrolyte (30.7%) than that formed in LSE (27.1%). As organic species have carbon as their backbone, a higher amount of C in the CEI indicates more organic components and fewer inorganic components. In **Figure 5b**, the O 1s spectral data show a stronger lattice oxygen signal in the LSE compared to that in the LP57 electrolyte. The quantitative analysis

of O in **Figure 5e** shows that the detectable lattice O from LNMO is 1.6% for LSE. The detectable bulk O from LNMO indicates a thinner CEI was formed on the positive electrode, which also implies fewer side reactions on the electrolyte and LNMO interface during cycling. These results indicate that the LSE helps form a thinner CEI with more inorganic components on the surface of LNMO.<sup>[36]</sup>

In the F 1s spectra (**Figure 5c**), the cycled LNMO electrode in the LSE shows a stronger signal of LiF ( $\approx 686.5$  eV) than that in LP57. The atomic ratio of this component increases from 3.0% (LP57) to 24.0% (LSE), as shown in **Figure 5e**. Li<sub>x</sub>PF<sub>y</sub>O<sub>z</sub> is also found in both samples, and the existence of Li<sub>x</sub>PF<sub>y</sub>O<sub>z</sub> in the CEI can also be identified from the O 1s spectra at  $\approx 535.5$  eV (**Figure 5b**) and the P 2p spectra at  $\approx 136$  eV (**Figure 5d**). The inclusion of Li<sub>x</sub>PF<sub>y</sub>O<sub>z</sub> in the CEI helps maintain stable performance in high-voltage applications (up to 4.8 V) and it prevents adverse side reactions at the CEI, allowing for better cycling performance and capacity retention.<sup>[55]</sup> The observed differences in the distribution of Li<sub>x</sub>PF<sub>y</sub>O<sub>z</sub> species between the LP57 and LSE samples can be attributed to their distinct electrolyte compositions and degradation pathways.<sup>[56,57]</sup> In the LP57 electrolyte, the simpler single-salt formulation leads to greater bulk

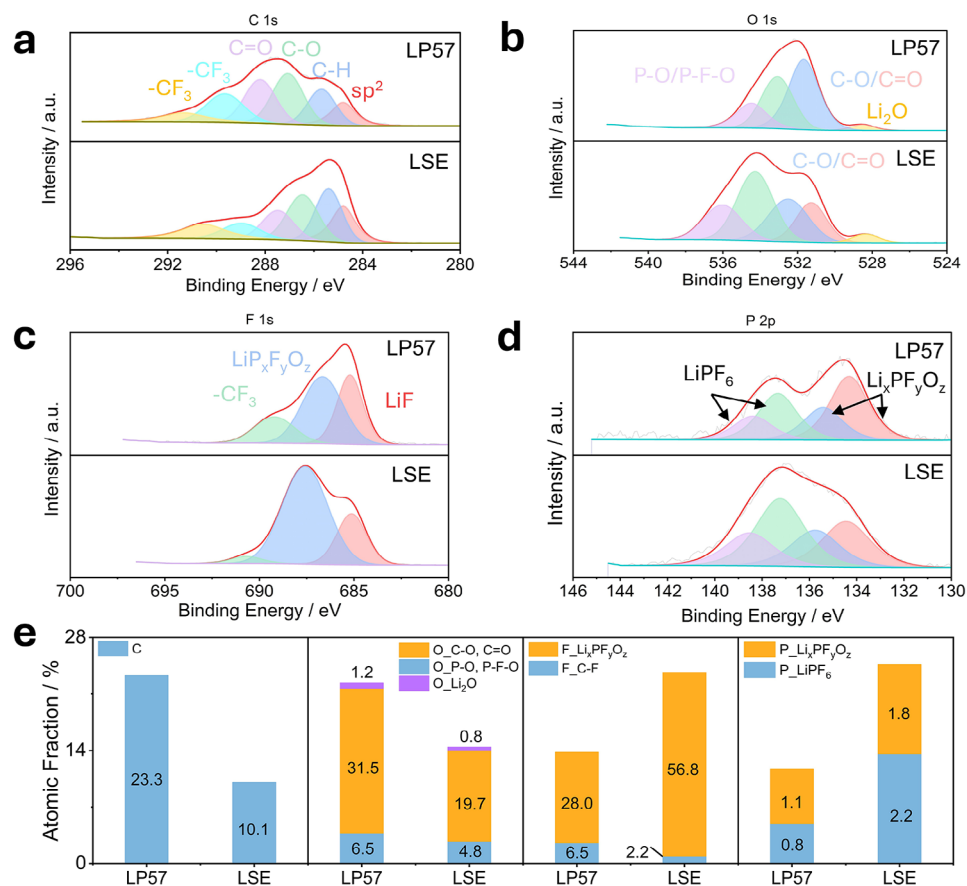


**Figure 6.** XPS characterization of cycled Li anode. a–d) XPS data of (a) C 1s, (b) O 1s, (c) F 1s, and (d) P 2p for the SEI on the Li surface. e) Quantitative analysis of different components derived from the XPS data.

decomposition of  $\text{LiPF}_6$ , resulting in a higher concentration of F in  $\text{Li}_x\text{PF}_y\text{O}_z$  species formed through reactions with unstable SEI components.<sup>[56]</sup> In contrast, the LSE electrolyte, which incorporates non-solvating TTE, suppresses extensive  $\text{LiPF}_6$  degradation in the SEI. However, the reduced electrolyte degradation under the localized saturated effect at the CEI leads to an accumulation of more LiF species within the CEI.<sup>[56]</sup> This distinction highlights the role of the localized saturated effect in influencing both the stability of the electrolyte and the distribution of decomposition products. Also, it is believed that the *in situ* formed LiF-rich CEI layer is an ideal shield to protect the surface of LNMO from further reactions with the electrolyte without reducing the ion transport kinetics.<sup>[58]</sup> These protective species in the CEI protect LNMO from the attack by HF and other free radical groups in the electrolyte, reducing the loss of oxygen and surface reconstruction into the disordered NiO-like rock salt phase.<sup>[59]</sup>

The composition of SEI formed on Li anodes was also characterized by XPS (Figure 6a–d), and the atomic ratios of different species of the SEI derived from the XPS data were summarized in Figure 6e. Figure 6a suggests that the SEI formed with the LSE has a lower concentration of carbon (10.1%) than that formed with the LP57 electrolyte (23.3%), indicating the SEI formed with the LSE is inorganic-rich. In Figure 6b,e, the O 1s spectral data show a stronger  $\text{Li}_2\text{O}$  signal in the LP57 (1.2%) com-

pared to that in the LSE (0.8%) electrolyte, suggesting more electrolyte decomposition residual on the SEI of Li anode in LP57.<sup>[57]</sup> The reduced C and P atomic ratio in the SEI also verified that LSE reduced the decomposition of solvents and  $\text{PF}_6^-$  in the electrolyte (Figure 6e). Besides, the SEI formed with the LSE shows a stronger signal of LiF and  $\text{Li}_x\text{PF}_y\text{O}_z$  ( $\approx 685.5$  eV) than that of LP57 (Figure 6c, Supporting Information). The atomic ratio of these components increases from 28.0% (LP57) to 56.8% (LSE), as shown in Figure 6e. The existence of more  $\text{Li}_x\text{PF}_y\text{O}_z$  in the SEI formed with the LSE can also be observed from the P 2p spectrum at  $\approx 134$  eV (Figure 6d). The inorganic-rich components in the SEI, i.e., LiF and  $\text{Li}_x\text{PF}_y\text{O}_z$  are believed to be beneficial to Li metal, leading to improved cycling stability of the cells with the LSE.<sup>[36]</sup> In addition, the degraded  $\text{LiPF}_6$  species, i.e.,  $\text{Li}_x\text{PF}_y\text{O}_z$ , have been demonstrated to scavenge transition metals and suppress electrode crosstalk.<sup>[60]</sup> The Mn dissolution has been recognized as one of the main factors of the degradation of the LNMO cathode material.<sup>[26]</sup> The Mn dissolved in the electrolyte will lead to signals on the Li anode. Figure S16 (Supporting Information) illustrates the Mn 2p spectra of the cycled Li anode harvested from Li|LNMO cells. There is a noticeable Mn signal on the Li metal tested in the LP57 electrolyte whereas no Mn signal can be observed in the one tested with LSE, suggesting that the LSE inhibits Mn dissolution from LNMO during long-term cycling.

### 3. Conclusion

This study uncovers the  $\text{Li}^+$  solvation structures in  $\text{LiPF}_6$ -based electrolytes with different salt concentrations through combined experimental characterizations and computational simulations. We found that “non-solvating” TTE diluent has a non-negligible impact on  $\text{Li}^+$  solvation structure, which agrees with recent findings that show the TTE diluent affects the solvation structure of  $\text{Li}^+$  cations in the LHCEs. Introducing TTE diluent changes the  $\text{Li}^+$  solvation environment by promoting  $\text{PF}_6^-$  coordination in the first solvation shell at the expense of EC and EMC solvent coordination. Compared to EC, more EMC molecules are pushed out of the first solvation shell by adding TTE. The unique  $\text{Li}^+$  solvation structure in LSE results in its high-voltage stability, and we demonstrate its excellent compatibility with 4.85 V high-voltage LNMO spinel cathode materials. The improved compatibility comes from the high-voltage stability of the LSE and the beneficial species formed at the surface of LNMO electrodes. These findings advance our understanding of high-voltage electrolytes and highlight the importance of selecting appropriate diluents in developing electrolytes to improve the stability and longevity of LIBs.

### 4. Experimental Section

**Materials Preparation:** The LP57 electrolyte consisted of 1 M  $\text{LiPF}_6$  in a solvent containing a 3:7 weight ratio of EC and EMC (purchased from Gotion). The SE consisted of 2.5 M  $\text{LiPF}_6$  (purchased from Gotion) dissolved in the LP57 electrolyte purchased from Gotion. The LSE was prepared by adding TTE (SynQuest, purity 99%) into the SE electrolyte with a volume ratio of 2:1 (TTE:SE). The LNMO cathode with a loading of  $15 \text{ mg cm}^{-2}$  (A-C024) and LTO anode (A-A020) are kindly provided by the CAMP facility from Argonne National Lab. The LNMO cathode ( $2 \text{ mg cm}^{-2}$ ) slurry was prepared by mixing 80 wt% LNMO (AOT, Xiamen), 10 wt% conductive carbon (super P), and 10 wt% PVDF in N-methyl pyrrolidine solvent. The resulting slurry was coated on an Al foil and dried in a vacuum furnace at  $80^\circ\text{C}$  overnight and then calendared.

**Electrochemical Performance Characterization:** CR2032-type coin cells were assembled in an Argon-fill glovebox with an  $\text{O}_2$  and  $\text{H}_2\text{O}$  level below 1 ppm. LNMO cathode, polyethylene separator from AOT, and Li-metal anode (diameter: 15.6 mm, thickness: 0.45 mm) were sandwiched together with  $75 \mu\text{l}$  electrolyte and crimped within the coin cell casings. Cycling tests were carried out with the Neware Battery Testing System (CT-4008Tn). The cells were cycled at a C/3 ( $1\text{C} = 135 \text{ mA g}^{-1}$ ) rate from 3.5 to 4.85 V three times before conducting the cycling tests. The self-discharge test was also carried out with the Neware Battery Testing System. Fully charged cells were stored inside the Neware environmental chamber at  $45^\circ\text{C}$  for 100 h, followed by a discharge at a C/10 rate of 3.5 V.

Linear sweep voltammetry scans were recorded in  $\text{Li|Al}$  cells with a Biologic potentiostat SP150 from 3.0 to 5.5 V with scan rates of  $1 \text{ mV s}^{-1}$ . The ionic conductivity of electrolytes is tested in  $\text{Li|Li}$  symmetric cells. The  $\text{Li}^+$  transference number of electrolytes is calculated using the method provided in this paper.<sup>[61]</sup> The EIS experiments were conducted using a Biologic potentiostat SP150, with a frequency range of 1 MHz to 10 mHz and a perturbation amplitude of 10 mV. Similarly, the direct current polarization experiments were carried out with the same potentiostat, applying a constant voltage bias of 10 mV until the current reached a steady state.

**Materials Characterization:** The XPS measurements were collected on cycled LNMO and Li electrodes with a Kratos Axis Ultra DLD spectrometer with an Al  $K\alpha$  radiation (1486.6 eV) excitation source. Aged cells were disassembled inside an Argon-filled glovebox to harvest the electrode samples, which were loaded into an in-house transfer chamber (patent num-

ber US9945761) inside the glovebox to avoid air exposure during sample transfer. Regions scans were performed with a step size of 0.1 eV. The adventitious carbon peak at 248.8 eV was used for calibration.

**Molecular Dynamics Simulation:** The classical molecular dynamics simulation was carried out in OpenMM<sup>[62]</sup> and executed with the atomate2 workflow management software. The Sage<sup>[63]</sup> force field was used to describe the intermolecular forces among molecules in the system with the LJ cutoff distances for the simulations set to 0.9 nm. The partial charges are calculated with the empirical AM1BCC<sup>[64]</sup> method. For each system, 1000 molecules are packed within a periodic box using PACKMOL according to the desired molar ratio, exact amounts shown below. All the charged species are charge-scaled by a factor of 0.8 since the nonpolarizable force field used for simulations will significantly overestimate ion pairing.<sup>[65]</sup> The system was equilibrated with the NPT ensemble at 298 K and 1 atm for 0.2 ns and then subjected to a 1.5 ns annealing. Annealing started by increasing the temperature to 400 K in 0.5 ns, followed by holding the temperature at 400 K for 0.5 ns, and then decreasing the temperature to 298 K in 0.5 ns. Finally, the annealed system was simulated with the NVT ensemble for 5 ns at 298 K to collect the production trajectory. The solvation calculations were performed with MDAnalysis<sup>[66]</sup> and SolvationAnalysis.<sup>[67]</sup>

### Supporting Information

Supporting Information is available from the Wiley Online Library or from the author.

### Acknowledgements

This work was supported by the U.S. Department of Defense's Office of Industrial Base Policy and its Manufacturing Capability Expansion and Investment Prioritization (MCEIP) office funding of the Batteries and Energy to Advance Commercialization and National Security (BEACONS) at the University of Texas at Dallas. L.S. acknowledges the New Faculty startup funding provided by The University of Texas at Dallas. The authors thank Dr. Hugo Celio at UT Austin for his assistance with the XPS measurement. The acquisition of the VersaProbe-IV XPS at UT-Austin was supported by the National Science Foundation Major Research Instrumentation program (Grant No. 2117623). The  $15 \text{ mg cm}^{-2}$  LNMO and  $11.5 \text{ mg cm}^{-2}$  LTO electrodes used in this work were produced by Argonne National Laboratory's Cell Analysis, Modeling, and Prototyping (CAMP) Facility, which is supported by the U.S. Department of Energy's Vehicle Technologies Office (VTO).

### Conflict of Interest

The authors declare no conflict of interest.

### Data Availability Statement

The data that support the findings of this study are available from the corresponding author upon reasonable request.

### Keywords

diluent, electrolytes, lithium-ion batteries, LNMO cathode, MD simulation, solvation structures

Received: February 18, 2025

Revised: March 28, 2025

Published online:

- [1] K. Xu, *Chem. Rev.* **2004**, *104*, 4303.
- [2] W. Bao, W. Yao, Y. Li, B. Sayahpour, B. Han, G. Raghavendran, R. Shimizu, A. Cronk, M. Zhang, W. Li, Y. S. Meng, *Energy Environ. Sci.* **2024**, *17*, 4263.
- [3] Q. Zhong, A. Bonakdarpour, M. Zhang, Y. Gao, J. R. Dahn, *J. Electrochem. Soc.* **1997**, *144*, 205.
- [4] X. L. Xu, S. X. Deng, H. Wang, J. B. Liu, H. Yan, *Nanomicro Lett* **2017**, *9*, 22.
- [5] T. F. Yi, J. Mei, Y. R. Zhu, *J. Power Sources* **2016**, *316*, 85.
- [6] C. Lin, J. Li, Z. W. Yin, W. Huang, Q. Zhao, Q. Weng, Q. Liu, J. Sun, G. Chen, F. Pan, *Adv. Mater.* **2024**, *36*, 32.
- [7] S. Choi, W. Feng, Y. Xia, *ACS Omega* **2024**, *9*, 18688.
- [8] F. Nobili, F. Croce, R. Tossici, I. Meschini, P. Reale, R. Marassi, *J. Power Sources* **2012**, *197*, 276.
- [9] J. Wang, W. Lin, B. Wu, J. Zhao, *Electrochim. Acta* **2014**, *145*, 245.
- [10] S. Y. Lee, J. H. Park, J. H. Cho, S. B. Kim, W. S. Kim, S. Y. Lee, *J. Mater. Chem.* **2012**, *22*, 12574.
- [11] M. C. Kim, S. H. Kim, V. Aravindan, W. S. Kim, S. Y. Lee, Y. S. Lee, *J. Electrochem. Soc.* **2013**, *160*, A1003.
- [12] Y. Wang, Q. Peng, G. Yang, Z. Yang, L. Zhang, H. Long, Y. Huang, P. Lu, *Electrochim. Acta* **2014**, *136*, 450.
- [13] G. R. Hu, J. C. Cao, Z. D. Peng, Y. B. Cao, K. Du, *Electrochim. Acta* **2014**, *149*, 49.
- [14] S. Yang, J. Chen, Y. Liu, B. Yi, *J Mater Chem A Mater* **2014**, *2*, 9322.
- [15] L. Zhou, D. Zhao, X. Lou, *Angewandte Chemie – International Edition* **2012**, *51*, 239.
- [16] N. Arun, V. Aravindan, S. Jayaraman, N. Shubha, W. C. Ling, S. Ramakrishna, S. Madhavi, *Nanoscale* **2014**, *6*, 8926.
- [17] T. Dong, H. Zhang, Y. Ma, J. Zhang, X. Du, C. Lu, X. Shangguan, J. Li, M. Zhang, J. Yang, X. Zhou, G. Cui, *J Mater Chem A Mater* **2019**, *7*, 24594.
- [18] T. Dong, P. Mu, S. Zhang, H. Zhang, W. Liu, G. Cui, *Electrochem. Energy Rev.* **2021**, *4*, 545.
- [19] P. Mu, H. Zhang, H. Jiang, T. Dong, S. Zhang, C. Wang, J. Li, Y. Ma, S. Dong, G. Cui, *J. Am. Chem. Soc.* **2021**, *143*, 18041.
- [20] J. Mu, A. Wei, X. Li, R. He, L. Sun, P. Liu, X. Bai, L. Zhang, X. Zhang, Z. Liu, J. Gao, *J. Power Sources* **2024**, *611*, 234707.
- [21] Y. Huang, Y. Li, C. Tan, Z. Huang, Q. Pan, Y. Chu, F. Zheng, H. Wang, Q. Li, *ACS Appl. Energy Mater.* **2022**, *5*, 639.
- [22] X. Y. Fan, M. Liu, T. L. Chen, W. Hao, Z. Cao, N. Jiang, Q. Liu, Y. H. Feng, H. Qin, S. F. Chen, S. Liu, X. Ji, Y. Xiao, S. Chou, P. F. Wang, *Adv. Funct. Mater.* **2024**, *34*, 2400996.
- [23] Z. Zou, H. Xu, H. Zhang, Y. Tang, G. Cui, *ACS Appl. Mater. Interfaces* **2020**, *12*, 21368.
- [24] S. Lin, H. Hua, Z. Li, J. Zhao, *ACS Appl. Mater. Interfaces* **2020**, *12*, 33710.
- [25] S. P. Kühn, K. Edström, M. Winter, I. Cekic-Laskovic, *Adv. Mater. Interfaces* **2022**, *9*, 2102078.
- [26] R. Amin, N. Muralidharan, R. K. Petla, H. Ben Yahia, S. A. Jassim Al-Hail, R. Essehli, C. Daniel, M. A. Khaleel, I. Belharouak, *J. Power Sources* **2020**, *467*, 228318.
- [27] Z. Cui, N. Khosla, T. Lai, J. Narayan, A. Manthiram, *ACS Applied Materials and Interfaces* **2023**, *15*, 1247.
- [28] X. Cao, X. He, J. Wang, H. Liu, S. Röser, B. R. Rad, M. Evertz, B. Streipert, J. Li, R. Wagner, M. Winter, I. Cekic-Laskovic, *ACS Appl. Mater. Interfaces* **2016**, *8*, 25971.
- [29] S. T. Oyakhire, S. L. Liao, S. B. Shuchi, M. S. Kim, S. C. Kim, Z. Yu, R. A. Vilá, P. E. Rudnicki, Y. Cui, S. F. Bent, *Nano Lett.* **2023**, *23*, 7524.
- [30] E. R. Fadel, F. Faglioni, G. Samsonidze, N. Molinari, B. V. Merinov, W. A. Goddard, J. C. Grossman, J. P. Mailoa, B. Kozinsky, *Nat. Commun.* **2019**, *10*, 3360.
- [31] M. Li, C. Wang, K. Davey, J. Li, G. Li, S. Zhang, J. Mao, Z. Guo, *Smart-Mat* **2023**, *4*, 1185.
- [32] X. Ren, L. Zou, X. Cao, M. H. Engelhard, W. Liu, S. D. Burton, H. Lee, C. Niu, B. E. Matthews, Z. Zhu, C. Wang, B. W. Arey, J. Xiao, J. Liu, J. G. Zhang, W. Xu, *Joule* **2019**, *3*, 1662.
- [33] S. Perez Beltran, X. Cao, J. G. Zhang, P. B. Balbuena, *Chem. Mater.* **2020**, *32*, 5973.
- [34] X. Cao, P. Gao, X. Ren, L. Zou, M. H. Engelhard, B. E. Matthews, J. Hu, C. Niu, D. Liu, B. W. Arey, C. Wang, J. Xiao, J. Liu, W. Xu, J. G. Zhang, *Proc Natl Acad Sci* **2021**, *118*, 2020357118.
- [35] H. Jia, J. Kim, P. Gao, Y. Xu, M. H. Engelhard, B. E. Matthews, C. Wang, W. Xu, *Angew. Chem.* **2023**, *135*, 202218005.
- [36] L. Su, E. Jo, A. Manthiram, *ACS Energy Lett.* **2022**, *7*, 2165.
- [37] L. Su, K. Jarvis, H. Charalambous, A. Dolocan, A. Manthiram, *Adv. Funct. Mater.* **2023**, *33*, 2213675.
- [38] J. B. Adamo, L. Su, A. Manthiram, *ACS Appl. Mater. Interfaces* **2023**, *15*, 15458.
- [39] R. Sim, L. Su, A. Manthiram, *Adv. Energy Mater.* **2023**, *13*, 2300096.
- [40] M. Yi, L. Su, A. Manthiram, *J Mater Chem A Mater* **2023**, *11*, 11889.
- [41] Y. Chen, Z. Yu, P. Rudnicki, H. Gong, Z. Huang, S. C. Kim, J. C. Lai, X. Kong, J. Qin, Y. Cui, Z. Bao, *J. Am. Chem. Soc.* **2021**, *143*, 18703.
- [42] O. Borodin, L. Suo, M. Gobet, X. Ren, F. Wang, A. Faraone, J. Peng, M. Olguin, M. Schroeder, M. S. Ding, E. Gobrogge, A. Von Wald Cresce, S. Munoz, J. A. Dura, S. Greenbaum, C. Wang, K. Xu, *ACS Nano* **2017**, *11*, 10462.
- [43] J. Self, N. T. Hahn, K. A. Persson, *Energy and Environmental Materials* **2022**, *7*, 2024.
- [44] D. S. Hall, J. Self, J. R. Dahn, *J. Phys. Chem. C* **2015**, *119*, 22322.
- [45] F. Ren, Z. Li, J. Chen, P. Huguet, Z. Peng, S. Deabate, *ACS Appl. Mater. Interfaces* **2022**, *14*, 4211.
- [46] L. Su, X. Zhao, M. Yi, H. Charalambous, H. Celio, Y. Liu, A. Manthiram, *Adv. Energy Mater.* **2022**, *12*, 2201911.
- [47] L. Xing, O. Borodin, *Phys. Chem. Chem. Phys.* **2012**, *14*, 12838.
- [48] T. Hou, K. D. Fong, J. Wang, K. A. Persson, *Chem. Sci.* **2021**, *12*, 14740.
- [49] L. Su, X. Zhao, M. Yi, H. Charalambous, H. Celio, Y. Liu, A. Manthiram, *Adv. Energy Mater.* **2022**, *12*, 2201911.
- [50] P. G. Bruce, C. A. Vincent, *J. Electroanal. Chem.* **1987**, *225*, 1.
- [51] K. Xu, *Commun. Mater.* **2022**, *3*, 31.
- [52] Z. Chen, H. Li, L. Wu, X. Lu, X. Zhang, *Chem. Rec.* **2018**, *18*, 350.
- [53] K. Xu, *Chem. Rev.* **2014**, *114*, 11503.
- [54] C. Han, Y. B. He, M. Liu, B. Li, Q. H. Yang, C. P. Wong, F. Kang, *J Mater Chem A Mater* **2017**, *5*, 6368.
- [55] F. Cheng, J. Xu, P. Wei, Z. Cheng, M. Liao, S. Sun, Y. Xu, Q. Li, C. Fang, Y. Lin, J. Han, Y. Huang, *Adv. Sci.* **2023**, *10*, 12.
- [56] E. W. C. Spotte-Smith, T. B. Petrocelli, H. D. Patel, S. M. Blau, K. A. Persson, *ACS Energy Lett.* **2023**, *8*, 347.
- [57] R. Azmi, F. Lindgren, K. Stokes-Rodriguez, M. Buga, C. Ungureanu, T. Gouveia, I. Christensen, S. Pal, A. Vlad, A. Ladam, K. Edström, M. Hahlin, *ACS Applied Materials and Interfaces* **2024**, *16*, 34266.
- [58] Q. Zhang, J. Pan, P. Lu, Z. Liu, M. W. Verbrugge, B. W. Sheldon, Y. T. Cheng, Y. Qi, X. Xiao, *Nano Lett.* **2011**, *16*, 2016.
- [59] S. Lee, L. Su, A. Mesnier, Z. Cui, A. Manthiram, *Joule* **2023**, *7*, 2430.
- [60] S. Klein, S. van Wickeren, S. Röser, P. Bärmann, K. Borzutzki, B. Heidrich, M. Börner, M. Winter, T. Placke, J. Kasnatscheew, *Adv. Energy Mater.* **2021**, *11*, 2003738.
- [61] L. Y. Lin, C. C. Chen, *J. Power Sources* **2024**, *603*, 234236.
- [62] P. Eastman, M. S. Friedrichs, J. D. Chodera, R. J. Radmer, C. M. Bruns, J. P. Ku, K. A. Beauchamp, T. J. Lane, L. P. Wang, D. Shukla, T. Tye, M. Houston, T. Stich, C. Klein, M. R. Shirts, V. S. Pande, *J. Chem. Theory Comput.* **2013**, *9*, 461.
- [63] S. Boothroyd, P. K. Behara, O. C. Madin, D. F. Hahn, H. Jang, V. Gapsys, J. R. Wagner, J. T. Horton, D. L. Dotson, M. W. Thompson,

- J. Maat, T. Gokey, L. P. Wang, D. J. Cole, M. K. Gilson, J. D. Chodera, C. I. Bayly, M. R. Shirts, D. L. Mobley, *J. Chem. Theory Comput.* **2023**, *19*, 3251.
- [64] M. Arba, Yamin, S. I., D. H. Tjahjono, *J Appl Pharm Sci* **2018**, *8*, 60.
- [65] B. J. Kirby, P. Jungwirth, *J. Phys. Chem. Lett.* **2019**, *10*, 7531.
- [66] R. Gowers, M. Linke, J. Barnoud, T. Reddy, M. Melo, S. Seyler, J. Domański, D. Dotson, S. Buchoux, I. Kenney, O. Beckstein, *Proceedings of the 15th Python in Science Conference* **2016**, 98.
- [67] O. A. Cohen, H. Macdermott-Opeskin, L. Lee, T. Hou, K. D. Fong, R. Kingsbury, J. Wang, K. A. Persson, *J Open Source Softw* **2023**, *8*, 5183.